

Optical read-out of the Néel vector in metallic antiferromagnet Mn₂Au

Vladimir Grigorev,^{1,2} Mariia Filianina,^{1,2} Stanislav Yu. Bodnar,^{1,3} Sergei Sobolev,¹
Nilabha Bhattacharjee,¹ Satya Bommanaboyena,¹ Yaryna Lytvynenko,¹ Yurii
Skourski,⁴ Dirk Fuchs,⁵ Mathias Kläui,^{1,2} Martin Jourdan,¹ and Jure Demsar^{1,2}

¹*Institute of Physics, Johannes Gutenberg University, 55128 Mainz, Germany*

²*Graduate School of Excellence Materials Science in Mainz, 55128 Mainz, Germany*

³*Walter Schottky Institut and Physics Department,*

Technische Universität München, 85748 Garching, Germany

⁴*Dresden High Magnetic Field Laboratory (HLD-EMFL),*

Helmholtz-Zentrum Dresden-Rossendorf, 01328 Dresden, Germany

⁵*Institute for Quantum Materials and Technologies (IQMT),*

Karlsruhe Institute of Technology, 76344 Eggenstein-Leopoldshafen, Germany

(Dated: June 25, 2021)

Metallic antiferromagnets with broken inversion symmetry on the two sublattices, strong spin-orbit coupling and high Néel temperatures offer new opportunities for applications in spintronics. Especially Mn₂Au, with high Néel temperature and conductivity, is particularly interesting for real-world applications. Here, manipulation of the orientation of the staggered magnetization, *i.e.* the Néel vector, by current pulses has been recently demonstrated, with the read-out limited to studies of anisotropic magnetoresistance or X-ray magnetic linear dichroism. Here, we report on the in-plane reflectivity anisotropy of Mn₂Au (001) films, which were Néel vector aligned in pulsed magnetic fields. In the near-infrared, the anisotropy is $\approx 0.6\%$, with higher reflectivity for the light polarized along the Néel vector. The observed magnetic linear dichroism is about four times larger than the anisotropic magnetoresistance. This suggests the dichroism in Mn₂Au is a result of the strong spin-orbit interactions giving rise to anisotropy of interband optical transitions, in-line with recent studies of electronic band-structure. The considerable magnetic linear dichroism in the near-infrared could be used for ultrafast optical read-out of the Néel vector in Mn₂Au.

I. INTRODUCTION

There is an increasing interest in antiferromagnetic (AFM) materials as active elements in future spintronics devices, including data storage applications [1–5]. This is motivated by the absence of net magnetization and the related stray fields, which limit the minimum distance between two bits, and thus leads to higher storage density compared to ferromagnets. Moreover, the inherently fast spin dynamics in AFMs, which takes place in the THz range [6–10], is orders of magnitude faster than typical spin dynamics in ferromagnetic materials (GHz range) [11]. The absence of net magnetization, however, makes the manipulation and read-out of magnetic order, which is given by the staggered magnetization, *i.e.* the Néel vector, generally difficult.

Recently, two fully compensated metallic antiferromagnets CuMnAs and Mn₂Au have been in the research focus. Here, the specific crystal and magnetic structure in combination with large spin-orbit coupling enable current driven manipulation of the Néel vector [12]. In particular, it was suggested that application of electric current pulses of the order of $10^8 - 10^9 \text{ A cm}^{-2}$ can rotate the Néel vector due to the bulk Néel spin-orbit torques (NSOT) [12]. Such current-driven switching was indeed demonstrated in metallic AFMs CuMnAs [13–15] and Mn₂Au [16–18], with pulse durations down to picoseconds, achieved by driving currents with pulsed THz radiation [19]. Note that the high Néel temperature ($\approx 1500 \text{ K}$) and high electrical conductivity [20, 21] make Mn₂Au

particularly interesting for real-world applications. In Mn₂Au the current pulses were shown to reorient only a fraction (up to 30 %) of the domains [17], implying further studies of the switching mechanisms as well as novel approaches are required.

The absence of net magnetization makes the efficient read-out of the direction of the Néel vector challenging. Indeed, the electrical read-out via the anisotropic magnetoresistance (AMR) and the planar Hall effect is well established [13, 16]. However, recent studies show that in Mn₂Au the AMR does not exceed 0.15 % [22]. Moreover, the read-out time in the AMR detection scheme is inherently limited by the electronics to timescales orders of magnitude larger than the intrinsic switching timescales [19]. Thus, using optical methods, which would enable fast read-out on the femtosecond scale, should be explored [23, 24]. While linear magneto-optic effects are commonly used to investigate magnetization and its dynamics in ferro- and ferri-magnets [25, 26], as well as in non-collinear antiferromagnets [27], the presence of the quadratic magneto-optical effects (Cotton-Mouton/Voigt effect) was demonstrated in several insulating AFMs [7, 28–30]. To probe the small changes in the refractive index due to the quadratic magneto-optical effects, polarimetry studies are commonly performed in the transmission geometry, since the changes in the optical phase accumulate over the optical path length within the material [28–30]. For metallic collinear AFM, with optical penetration depths on the order of tens of nanometers, the corresponding changes are small. Thus, for CuM-

nAs another approach has been recently demonstrated [31, 32]. Here, the thermomodulation aspect of the optical pump-probe technique has been used to detect small photoinduced changes in rotation of the polarization of the optical probe beam. Since such changes depend on the polarization of light with respect to the Néel vector, probe polarization dependence is used to determine the direction of the Néel vector [31, 32]. Indeed, similar approach has been recently used to study dynamics in metallic AFM Fe₂As [33] and insulating CoO [34]. Finally, we note, that several recent reports demonstrated large magneto-optical contrast also in ultrathin NiO [35–37] and CoO [38] films. However, in this case the origin of the magneto-optical contrast is in large magnetostriction.

In Mn₂Au, the recent angular-resolved photoemission study of Néel vector aligned Mn₂Au films demonstrated the breaking of the C_{4z} symmetry, a consequence of antiferromagnetic order and strong spin-orbit interaction [39]. In fact, a pronounced in-plane anisotropy of the electronic band structure is observed up to the binding energy of a few eV [39]. The existence of flat bands at the 1.5 eV binding energy, and their calculated anisotropy may present means to detect a substantial magnetic linear dichroism in the near-infrared (NIR) range.

Here, we report on near-infrared magnetic linear dichroism (MLD) measurements on Mn₂Au thin films, performed in reflectance geometry at room temperature. To determine the magnitude of the MLD we investigate Mn₂Au films whose staggered magnetization (Néel vector) was aligned using pulsed magnetic field [22]. The MLD in the NIR range is found to be $\approx 0.6\%$, about four times larger than the observed anisotropic magnetoresistance in Mn₂Au [22]. The comparatively large MLD suggests it originates from the anisotropy in the interband absorption as a result of C_{4z} symmetry breaking.

II. RESULTS AND DISCUSSION

A. Mn₂Au thin films

Mn₂Au has a body-centered tetragonal crystal structure, whose unit cell is depicted in Fig. 1(d). It is an easy plane (001) AFM, with a strong out-of plane hard axis and a weak in-plane magnetic anisotropy. The spin orientations in adjacent layers are presented by arrows, with the Néel vector pointing along the easy [110] directions [20, 21, 40].

The *c*-axis epitaxial Mn₂Au thin film is grown on r-cut (1 $\bar{1}$ 02) Al₂O₃ substrate, with the lateral size of 10×10 mm² and thickness of 530 μm by the radio-frequency magnetron sputtering at 600 °C - see Ref. [21,37] for fabrication details. To ensure epitaxial growth, a 45 nm thick Mn₂Au film is deposited on a 20 nm thick (001) Ta buffer layer. To protect the surface, a 2 nm Al layer is deposited on Mn₂Au, forming an aluminum-oxide capping layer. Mn₂Au grows epitaxially with [110] and [1 $\bar{1}$ 0]

axes parallel to the substrate edges, which are along the [010]_s and [211]_s directions of r-cut Al₂O₃. As elaborated in Appendix B, the *c*-axis of Mn₂Au films grown on r-cut Al₂O₃ is tilted by 2-3° towards the [010]_s direction.

As previously demonstrated [22, 39, 41, 42], the application of magnetic field, exceeding 30-50 T results in the aligning the Néel vector along one of the easy axes, perpendicular to the applied magnetic field [41]. While such a "polarization" of the film may be incomplete, *i.e.* there is still a small fraction of orthogonally polarized domains, it is quasi permanent [22, 39, 41].

To perform systematic measurements, the as-grown sample is cut into 5×5 mm² pieces. The three pieces investigated are labeled with letters A-C. Sample A is in the as-prepared state, *i.e.* in a multidomain configuration, and is used as a reference. Samples B and C are Néel vector aligned [22, 39, 41] in the pulsed magnetic field of 60 T along the different, yet crystallographically equivalent {110} directions, as shown in the middle panel of Fig. 1. Throughout this work the default film orientation is such that $x \parallel [010]_s$ and $y \parallel [211]_s$.

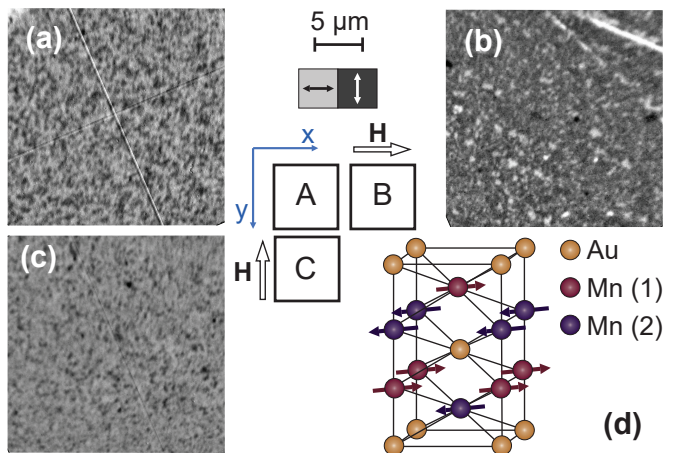


FIG. 1. The sample layout and the XMLD-PEEM images of samples A-C, shown in panels (a)-(c), respectively. Mn₂Au grows epitaxially with [110] and [1 $\bar{1}$ 0] axes parallel to the substrate edges which are along [010]_s (*x*) and [211]_s (*y*) axes of the r-cut sapphire. Sample A was as grown, while samples B and C were orthogonally polarized in the 60 T pulsed magnetic field. The directions of the applied magnetic field and the corresponding Néel vector directions are shown in the center, together with the scale of the XMLD-PEEM images. The contrast shows the two types of magnetic domains with the Néel vector along the two orthogonal easy axes: [110] and [1 $\bar{1}$ 0]. In the as-prepared sample A, roughly equal volume fraction of both types of domains is observed, while the aligned samples B and C display mostly one type of the domains. (d) The unit cell of Mn₂Au, with spin orientations in adjacent layers shown by arrows.

B. X-ray magnetic linear dichroism in polarized Mn₂Au films

Prior to optical studies the AFM domain patterns of all samples are first imaged by X-ray magnetic linear dichroism photoemission electron microscopy (XMLD-PEEM). The XMLD-PEEM imaging of the AFM domains is performed at room temperature at the SIM beamline of the Swiss Light Source. The sample is illuminated by linearly polarized X-rays with the polarization in the sample plane and the angle of incidence of 16°. The XMLD contrast was obtained by using the two-energy mode, as described in detail in Ref.[39]. Here the energies $E_1 = 639$ eV and $E_2 = 638.2$ eV were used, which correspond to the maximum and minimum of the XMLD [42].

The XMLD-PEEM images of all samples are shown in Fig. 1, demonstrating that samples *B* and *C* have orthogonally oriented Néel vector. In particular, each of the polarized samples has mostly one type of AFM domains, with narrow worm-like domains of the other type, similarly to earlier reports [41, 42]. The sample *A*, on the other hand, has about equal density of the domains of both types. Hence, sample *A* is used as a reference in optical dichroism measurements.

C. Magnetic linear dichroism in the near-infrared

General symmetry considerations

In a tetragonal easy-plane system like Mn₂Au a symmetry-based phenomenological model of the quadratic magneto-optical effect generally implies two possible contributions to the MLD: an isotropic and an anisotropic [28]. The isotropic contribution does not depend on the direction of the Néel vector within the plane, and can be observed when light is propagating along the two-fold symmetry axis of the crystal (here, we are considering the crystal symmetry only). The anisotropic MLD does depend on the direction of the Néel vector [29] and is present when the light propagates along the fourfold symmetry axis. It is the anisotropic component, that can be used to determine the Néel vector orientation in a collinear AFM.

The corresponding dielectric tensor of an AFM with the tetragonal crystal structure and the Néel vector perpendicular to the fourfold symmetry axis (*i.e.* within the easy $a - b$ plane), can be written as [28]:

$$\begin{aligned}
 \epsilon_{xx} &= \epsilon_{\perp} + \lambda_1 \vec{L}^2 + \frac{1}{2} \lambda_3 (L_x^2 - L_y^2) - 2\lambda_4 L_x L_y \\
 \epsilon_{yy} &= \epsilon_{\perp} + \lambda_1 \vec{L}^2 - \frac{1}{2} \lambda_3 (L_x^2 - L_y^2) + 2\lambda_4 L_x L_y \\
 \epsilon_{zz} &= \epsilon_{\parallel} + \lambda_2 \vec{L}^2 \\
 \epsilon_{xy} = \epsilon_{yx} &= \frac{1}{2} \lambda_3 (L_x^2 - L_y^2) + 2\lambda_4 L_x L_y \\
 \epsilon_{xz} = \epsilon_{zx} = \epsilon_{yz} = \epsilon_{zy} &= 0
 \end{aligned} \tag{1}$$

Here ϵ_{\perp} and ϵ_{\parallel} are the in-plane and out-of-plane dielectric constants in the absence of magnetic order, \vec{L} is the Néel vector and λ_i are the phenomenological coefficients related to the MLD. Given the two possible directions of the Néel vector in Mn₂Au, we choose the z -axis to be along the fourfold [001] axis, while x and y coincide with [110] and $[\bar{1}\bar{1}0]$ crystallographic axes. The difference between $\epsilon_{xx/yy}$ and ϵ_{zz} is governed by $\epsilon_{\perp} - \epsilon_{\parallel}$, yet includes also the component proportional to \vec{L}^2 , *i.e.* the so called isotropic component to the MLD (the term proportional to \vec{L}^2 is likely negligible compared to $\epsilon_{\perp} - \epsilon_{\parallel}$). The difference $\epsilon_{\perp} - \epsilon_{\parallel}$ may lead to the reflectivity-anisotropy in non-normal incidence configuration (see Appendix B).

Experimental approach

The goal of the experiment is to determine the anisotropic magnetic contribution to dichroism, given by $\epsilon_{xx} - \epsilon_{yy}$, which is proportional to phenomenological constants λ_3 and λ_4 and depends on the (in-plane) Néel vector orientation. Such a MLD is expected to be in the range of 10^{-3} and could be overshadowed by extrinsic non-magnetic effects such as strain. In particular, in the case of an additional lattice distortion in the ab -plane due to strain, ϵ_{\perp} (and λ_1 as well) would be different for the x and y directions, leading to reflectivity-anisotropy in the ab -plane unrelated to the magnetic order (see the discussion in Appendix B). Furthermore, such extrinsic contributions may vary from sample to sample due to slight variation of substrate properties such as miscut. Thus, to unambiguously determine the MLD, measurements on different magnetically aligned parts of the same film are performed.

Optical dichroism is studied using a setup shown in Fig. 2(a) - for details see Appendix A. The measurements are performed at room temperature. We use the 852 nm laser diode and a Photo-Elastic modulator (PEM) to modulate the polarization of incoming light between the two orthogonal linear polarizations: s -polarized (vertical) and p -polarized (horizontal). The Mn₂Au films were mounted such that their easy axes are along the horizontal/vertical directions, which correspond to x and y directions of ϵ_{ij} . The light reflected from the sample is focused onto a photodiode and the AC signal is recorded using a digital oscilloscope. Measurements at multiple

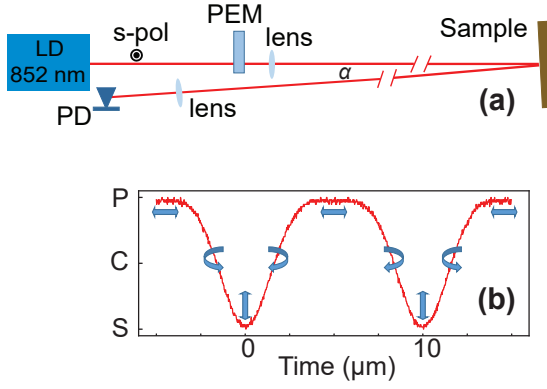


FIG. 2. (a) Schematic of the experimental setup (top view). The laser diode (LD) is vertically polarized (*s*-polarized). The polarization is modulated by the photo-elastic modulator (PEM) operating at 50 kHz. The distance between the LD and the sample is about 2.5 m, while the photodiode (PD) is mounted about 3 cm from the laser output, giving the incidence angle $\alpha/2 \approx 0.34^\circ$. Panel (b) presents the time evolution of the light intensity on the PD, when a polarizer is placed in front of the PD selecting the horizontal (*p*-polarized) signal (the modulation period is 10 μ s). The blue arrows represent the polarization states at given times, varying between vertical (*s*) and horizontal (*p*) polarizations that are along the $[110]/[\bar{1}\bar{1}0]$ crystalline axes of Mn_2Au .

positions on each of the three samples are performed (the laser spot diameter on the sample was about 500 μm) and averaged to minimize systematic errors.

Disentanglement of the MLD and structural dichroism

In our experimental geometry, with *x/y* corresponding to horizontal/vertical light polarizations, the MLD, given by $\epsilon_{xx} - \epsilon_{yy}$ in Eq. (1), should result in a difference between reflectivities of the *s*- and *p*-polarized light. However, the weak modulation of the intensity of the reflected light is also expected due to effects related to the operation of the PEM, as well as due to structural/strain anisotropy. Thus, the modulation of light intensity on the photo-diode, $\Delta I = \frac{\Delta R}{R}$ (the reflectivity, *R*, of Mn_2Au at 852 nm is 0.52 +/- 0.01), can be expressed as:

$$\Delta I_i(\phi) = D_0 P(\phi) + D_{mag}^i P(\phi) + D_{str}^i P(\phi). \quad (2)$$

Here D_0 is the contribution to the signal related to the PEM operation and slight misalignment of optical components (present also when measuring uncoated gold mirror as a reference). D_{mag}^i is the amplitude related to the MLD of the sample, where $i = A - C$. Finally, D_{str}^i is the amplitude of the dichroism caused by structural effects, such as strain. Here, we assume that in the first approximation the structural/strain dichroism is decoupled from D_{mag}^i , *i.e.* the strain does not affect the Néel vector. Thus, we assume D_{str}^i is independent on the Néel

vector direction, but depends on the sample orientation (see also Appendix B). Finally, $P(\phi)$ is a periodic function describing the polarization state of light after passing through the PEM - see Fig. 2(a). Since identical experimental geometry is used for all samples, D_0 is the same in all measurements. Moreover, given the samples *A-C* were cut from the same film, D_{str}^i should be identical to all samples, when mounted along the same direction with respect to the as-grown sample. Conversely, D_{str}^i should change sign when the sample is rotated by 90° around the C_4 axis, *i.e.* $D_{str}^i = -D_{str}^{i(90)}$. When considering the MLD, $D_{mag}^A \approx 0$, given the multidomain state on the length scale of the laser spot size of 500 μm . Finally, taking into account orthogonal direction of the Néel vector in the two magnetically aligned samples, it follows that $D_{mag}^B = -D_{mag}^C$. Under these assumptions the structural and magnetic contribution can be disentangled by the following referenced measurements:

$$D_{mag} P(\phi)/2 = \Delta I_B(\phi) - \Delta I_A(\phi) = \Delta I_A(\phi) - \Delta I_C(\phi) \quad (3)$$

$$D_{str} P(\phi) = \Delta I_A(\phi) - \Delta I_A^{(90)}(\phi) = \Delta I_B(\phi) - \Delta I_C^{(90)}(\phi) \quad (4)$$

Near-infrared magnetic linear dichroism in Mn_2Au

Fig. 3 presents the results of dichroism measurements, which are performed in sequence, under identical conditions. The dashed black line, representing the evolution of the polarization state - see Fig. 2(b) - is added to all panels as a guide to the eye. Fig. 3(a) presents the raw data, $\Delta I_i(\phi)$, taken on samples *A*, *B* and *C*. The complicated shape of the raw signal is largely a result of the optical elements of the setup, mainly the PEM. The PEM acts as a $\lambda \cdot \delta$ wave plate, where δ is modulated between $-1/2$ and $1/2$. This results in a sequence of polarization states *s-p-s-p-s* within one modulation period of the PEM (20 μ s). Note that between *s*- and *p*-polarizations, the light is circularly/elliptically polarized. Due to imperfections and asymmetry between the optical properties of the squeezed and elongated PEM crystal a modulation of the signal at 50 kHz is also observed.

To obtain the MLD component we first subtract the signal of the reference sample (as-prepared, *A*) from signals obtained on the magnetically polarized samples *B* and *C*, following Eq.(3). Moreover, as the MLD should give rise to a periodic modulation in reflectivity at the second harmonic of the PEM frequency, we fold the data recorded over two periods into the 10 μ s time window. The resulting variations are shown in Fig. 3(b). The differential signals do not have a complicated shape of the raw data as in Fig. 3(a), demonstrating that subtraction efficiently cancels out all system related modulations. Indeed, the shape of the differential signal follows the shape of the reference curve (dashed line). Furthermore, the absence of modulation of the differential signal

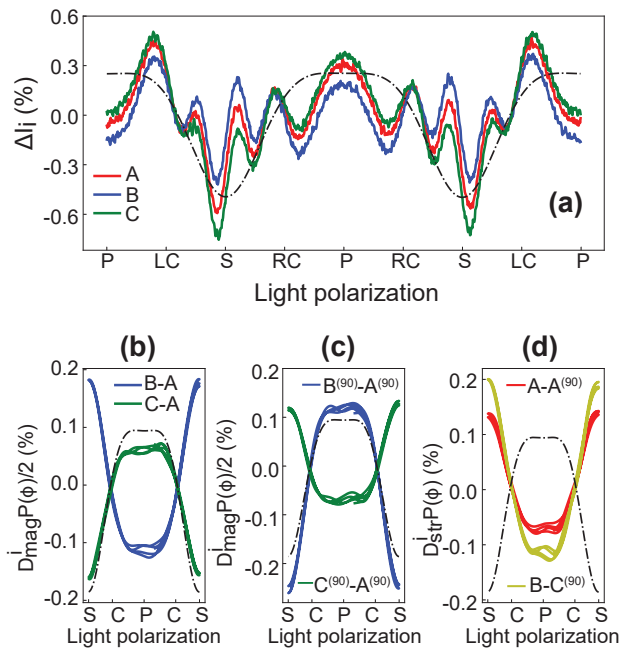


FIG. 3. Results of reflectivity anisotropy studies of Mn_2Au films with different orientations of the magnetic order. (a) The raw reflectivity modulation signals from all three samples, oriented in the same growth direction (raw data obtained on samples rotated by 90° are not shown). Here S, P, LC and RC stand for the s -polarized, p -polarized, and left and right circularly polarized light, respectively. The time window here is $20 \mu\text{s}$. Panels (b)-(d) present the differential signals, disentangling the MLD and structural contributions to reflectivity variation according to Eqs. (3) and (4). Here the traces have been folded into the $10 \mu\text{s}$ time window to emphasize the lack of circular dichroism, which should have a 50 kHz component. The modulation in (b) and (c) is a result of the MLD, while the modulation in (d) reflects the structural component to dichroism. Note that the modulation of reflectivity was recorded using a digital oscilloscope in the AC coupling mode. Thus, the zero baseline is automatically determined by the oscilloscope as the mean value of the periodic signal. Due to the asymmetry of the signal, the zero level does not correspond to the arithmetic average of the maximum and minimum. The asymmetry is a result of PEM operation, where the flat regions (here the light is p -polarized - see Figure 2(b)) correspond to the maximal retardation of the photo-elastic modulator.

at the 50 kHz PEM frequency clearly confirms the absence of circular dichroism. Fig. 3(c) presents the result obtained by the same approach for samples rotated by 90° around the C_4 axis. The fact that the differential signals $\Delta I_B^{(90)}(\phi) - \Delta I_A^{(90)}(\phi)$ and $\Delta I_C^{(90)}(\phi) - \Delta I_A^{(90)}(\phi)$ in Fig. 3(c) are phase-shifted by π underscores the MLD nature of the differential signals.

The MLD-induced change in reflectivity is given by the differences between the maxima and minima of the traces in Fig. 3 (b-c), multiplied by a factor of two (the signals shown in Fig. 3(b) and (c) are relative to the unpolarized reference sample A). The reflectivity is found to be

higher for the light polarized parallel to the staggered magnetization. The average value of the MLD induced reflectivity change from all data combined is $0.52 \pm 0.14\%$. We note, however, that it follows from Fig. 3(b) and (c) that the MLD extracted from $\Delta I_B(\phi) - \Delta I_A(\phi)$ and $\Delta I_B^{(90)}(\phi) - \Delta I_A^{(90)}(\phi)$ ($0.63 \pm 0.03\%$), is larger than the MLD extracted from $\Delta I_C(\phi) - \Delta I_A(\phi)$ and $\Delta I_C^{(90)}(\phi) - \Delta I_A^{(90)}(\phi)$ ($0.41 \pm 0.07\%$). This may suggest that the underlying microstructural strain favors the orientation of the Néel vector parallel to the c -axis tilt (parallel to the $[010]_s$ axis of the substrate), resulting in a partial polarization of the as grown reference sample A along the $[010]_s$ axis. Indeed, preliminary study using scanning electron microscopy with polarization analysis seem to support this observation [43].

Fig. 3(d) presents results of the measurements of structural dichroism. Following Eq.(4), for differences $\Delta I_A(\phi) - \Delta I_A^{(90)}(\phi)$ and $\Delta I_B(\phi) - \Delta I_C^{(90)}(\phi)$ the signal due to the MLD should cancel out and the remaining variation of reflectivity is due to the structural/strain effects. The extracted $D_{str} = 0.26 \pm 0.08\%$, with the reflectivity being larger for light polarized perpendicular to the direction of the c -axis tilt, i.e. parallel to the $[211]_s$ axis of the r-cut sapphire (see also Appendix B). Thus, the structural dichroism is about twice smaller than the MLD in Mn_2Au films on r-cut sapphire. Noteworthy, the value of D_{str} extracted from $\Delta I_A(\phi) - \Delta I_A^{(90)}(\phi)$ is again noticeably lower than the value extracted from $\Delta I_B(\phi) - \Delta I_C^{(90)}(\phi)$. This is consistent with the above suggestion that the as-grown sample is partially polarized along the $[010]_s$ axis of the substrate, resulting in a lower value of the extracted structural dichroism when monitoring $\Delta I_A(\phi) - \Delta I_A^{(90)}(\phi)$.

III. CONCLUSIONS

We demonstrate a pronounced magnetic linear dichroism in the NIR range in a collinear metallic antiferromagnet Mn_2Au at room temperature. The observed MLD of $\approx 0.6\%$ exceeds the value of AMR in Mn_2Au [22], recorded at liquid Helium temperatures, by about a factor of four. While no study on temperature dependence of the AMR in Mn_2Au has been performed thus far, one may expect that the increased electron-phonon and electron-magnon scattering give rise to a suppression of AMR at higher temperatures, as typically observed. Thus, the ratio between the MLD and AMR may in fact be even higher at room temperature.

Recent broadband terahertz study of several ferromagnets demonstrated AMR signals up to 30 THz [44], with the effect slowly decreasing with increasing frequency. The large difference between the observed MLD in the near-infrared and the AMR in Mn_2Au [22] implies the MLD in the near-infrared to be a result of the polarization dependent interband absorption. Indeed, the recent angular-resolved photoemission spectroscopy study

does show that the Néel vector orientation leads to a pronounced valence band asymmetry up to binding energies of several eV [39]. Thus, further systematic studies of MLD as a function of photon energy may reveal spectral ranges with even higher MLD.

In view of the recent studies, demonstrating a large magneto-optical contrast in ultrathin NiO [35–37] and CoO [38] films, it is tempting to estimate the polarization rotation angle, which corresponds to the observed MLD-induced reflectivity variation of $\approx 0.6\%$. Assuming the observed reflectivity change is dominated by the variation of the (interband) absorption coefficient, we estimate the polarization rotation angle for the light polarized at 45° away from the Néel vector to be ≈ 340 mdeg, about a factor of 2 larger than the reported value in CoO thin films [38] and more than a factor of 5 larger than the reported value in NiO thin films [35].

As a simple non-perturbative table-top experiment, the presented approach can be extended to imaging mode, enabling detection of Néel vector orientation with micrometer spatial resolution. Moreover, in view of potential applications of Mn₂Au, *e.g.* as a spintronic memory device, utilizing sequences of femtosecond optical pulses can provide read-out speeds matching the expected ultrafast switching times in antiferromagnetic memory devices.

ACKNOWLEDGMENTS

This work was funded by the Deutsche Forschungsgemeinschaft (DFG, German Research Foundation) Grant No. TRR 173 268565370 (project A05). This work received support from Horizon 2020 Framework Program of the European Commission under grant agreement No. 863155 (S-NEBULA). V.G. and M.F. acknowledge the financial support from the Graduate School of Excellence "Materials Science in Mainz" (DFG GSC 266 49741853). We acknowledge the Paul Scherrer Institut, Villigen, Switzerland for the beamtime allocation under proposal 20200977 at the SIM beamline of the SLS. The authors thank the SIM beamline staff for the technical support. We acknowledge valuable discussions with H.-J. Elmers, H. Gomonay, P. Grigorev and L. Šmejkal.

APPENDIX A: EXPERIMENTAL SETUP FOR OPTICAL DICHROISM

Our experimental setup is sketched in Fig. 2(a). For the non-cubic material, the experimental reflectivity-anisotropy can be a result of a finite angle of incidence. For the same reason, *i.e.* the difference in reflectivities of *p*- and *s*-polarized light, any dielectric mirrors need to be avoided in the beam path. Therefore, it is not possible to use normal incidence and to separate the reflected light using a semi-transparent dielectric mirror. To minimize such effects, the angle of incidence of $\alpha/2 \approx 0.34^\circ$

is used. Moreover, we use minimal number of the optical elements, with the only reflecting surface being the surface of the sample, as shown in Fig. 2(a).

We use the 852 nm laser diode and a Photo-Elastic modulator (PEM) from Hinds Instruments, which operates at the frequency of 50 kHz. The PEM is set to $\lambda/2$ retardation mode for 852 nm, resulting in a modulation of light polarization between *s*-polarized (vertical) and *p*-polarized (horizontal) at 100 kHz, the second harmonic of the PEM - see Fig. 2(b).

The laser intensity was 5 mW while the diameter of the laser spot on the sample was 500 μm . The laser heating in thin films is governed by the absorbed light intensity and the thermal properties of the substrate (sapphire in our case). The temperature increase of the illuminated region can be estimated using a simple steady-state heat diffusion model [45, 46]. Using the reflectivity of 0.52, thermal conductivity of sapphire at room temperature of 35 W/mK [47] we estimated, using Eq.(3) of Ref.[46], the steady state heating to be < 0.1 K. Thus, the laser heating can be neglected.

APPENDIX B: THE POSSIBLE ORIGINS OF STRUCTURAL DICHROISM

While our data clearly demonstrate the presence of a substantial MLD in Mn₂Au, there are two possible origins giving rise to the structural component of the measured reflectivity anisotropy - see Fig. 3(d). To address these, we first need to consider the specifics of the epitaxial film growth on r-cut sapphire using the Ta (001) buffer layer [21, 40].

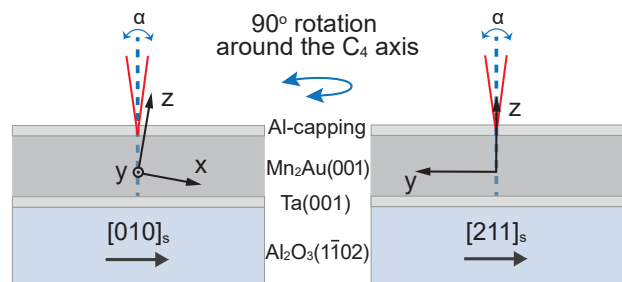


FIG. 4. Schematic of the sample layout in dichroism measurements for the two different orientations of the sample (left and right) with respect to the laser beam directions (red lines). Here *x* and *y* correspond to $[110]$ and $[1\bar{1}0]$ directions of Mn₂Au, while *z* is parallel to the *c*-axis, $[001]$. The tilt of the *c*-axis is highly exaggerated.

As elaborated elsewhere [17, 48], the *c*-axis of the Mn₂Au films grown on $(1\bar{1}02)$ Al₂O₃ is tilted with respect to the surface normal by about 2-3° (the tilt shows small variation from sample to sample). It turns out the the *c*-axis of the film tilts towards the $[010]_s$ axis of the substrate.

Given the tilted growth, the observed structural

dichroism could be a result of the experimental geometry - the effect is illustrated in Fig. 4. Namely, due to the tilt of the film's c -axis with respect to the surface normal, the rotation of sample by 90° (or equivalently by rotating the light polarization) changes the projection of the \vec{k} vector of light onto the c -axis. The difference between ϵ_\perp and ϵ_\parallel can thus give rise to reflectivity modulation. Unfortunately, due to the lack of data on (anisotropic) optical properties of Mn_2Au , this contribution cannot be estimated.

On the other hand, the observed dichroism can also be a result of the underlying strain as a result of the anisotropic thermal expansion of sapphire [49, 50]; such

an effect can not be neglected on the low-symmetry cut of the Al_2O_3 . Indeed, investigations of sample morphology using atomic force microscopy suggest breaking of the four-fold symmetry [40]. Considering the underlying strain to be responsible for the non-magnetic components of dichroism, its amplitude could roughly be estimated from D_{str} . Assuming a linear relation between D_{str} and the relative difference in the $[110]/[1\bar{1}0]$ lattice spacings the latter should be of the order of 0.1 %. Using the XRD measurements we are, however, unable to resolve such a weak asymmetry between the $[110]$ and $[1\bar{1}0]$ lattice spacings parameters, because of the rather large mosaicity of $\approx 0.5^\circ$ [21, 40].

-
- [1] I. Zutic, J. Fabian, and S. Das Sarma, Spintronics: Fundamentals and applications, *Rev. Mod. Phys.* **76**, 323 (2004).
- [2] A. H. MacDonald and M. Tsoi, Antiferromagnetic metal spintronics, *Phil. Trans. R. Soc. A.* **369**, 3098 (2011).
- [3] E. V. Gomonay and V. M. Loktev, Spintronics of antiferromagnetic systems (review article), *Low Temperature Physics* **40**, 17 (2014).
- [4] T. Jungwirth, X. Marti, P. Wadley, and J. Wunderlich, Antiferromagnetic spintronics, *Nature Nanotech* **11**, 231 (2016).
- [5] V. Baltz, A. Manchon, M. Tsoi, T. Moriyama, T. Ono, and Y. Tserkovnyak, Antiferromagnetic spintronics, *Rev. Mod. Phys.* **90**, 015005 (2018).
- [6] T. Kampfrath, A. Sell, G. Klatt, A. Pashkin, S. Mährlein, T. Dekorsy, M. Wolf, M. Fiebig, A. Leitenstorfer, and R. Huber, Coherent terahertz control of antiferromagnetic spin waves, *Nature Photonics* **5**, 31 (2011).
- [7] A. H. M. Reid, T. Rasing, R. V. Pisarev, H. A. Dürr, and M. C. Hoffmann, Terahertz-driven magnetism dynamics in the orthoferrite DyFeO_3 , *Applied Physics Letters* **106**, 082403 (2015).
- [8] K. Yamaguchi, M. Nakajima, and T. Suemoto, Coherent control of spin precession motion with impulsive magnetic fields of half-cycle terahertz radiation, *Phys. Rev. Lett.* **105**, 237201 (2010).
- [9] T. H. Kim, S. Y. Hamh, J. W. Han, C. Kang, C.-S. Kee, S. Jung, J. Park, Y. Tokunaga, Y. Tokura, and J. S. Lee, Coherently controlled spin precession in canted antiferromagnetic YFeO_3 using terahertz magnetic field, *Applied Physics Express* **7**, 093007 (2014).
- [10] M. Arana, F. Estrada, D. S. Maior, J. B. S. Mendes, L. E. Fernandez-Outon, W. A. A. Macedo, V. M. T. S. Barthem, D. Givord, A. Azevedo, and S. M. Rezende, Observation of magnons in Mn_2Au films by inelastic brillouin and raman light scattering, *Applied Physics Letters* **111**, 192409 (2017).
- [11] R. E. Camley, Z. Celinski, and R. L. Stamps, Magnetism of surfaces, interfaces, and nanoscale materials, *Handbook of Surface Science* **5**, 2 (2015).
- [12] J. Železný, H. Gao, K. Vybörný, J. Zemen, J. Mašek, A. Manchon, J. Wunderlich, J. Sinova, and T. Jungwirth, Relativistic néel-order fields induced by electrical current in antiferromagnets, *Physical review letters* **113**, 157201 (2014).
- [13] P. Wadley, B. Howells, J. Železný, C. Andrews, V. Hills, R. P. Campion, V. Novák, K. Olejník, F. Maccherozzi, S. Dhesi, *et al.*, Electrical switching of an antiferromagnet, *Science* **351**, 587 (2016).
- [14] M. J. Grzybowski, P. Wadley, K. W. Edmonds, R. Beardley, V. Hills, R. P. Campion, B. L. Gallagher, J. S. Chauhan, V. Novak, T. Jungwirth, F. Maccherozzi, and S. S. Dhesi, Imaging current-induced switching of antiferromagnetic domains in CuMnAs , *Phys. Rev. Lett.* **118**, 057701 (2017).
- [15] P. Wadley, S. Reimers, M. J. Grzybowski, C. Andrews, M. Wang, J. S. Chauhan, B. L. Gallagher, R. P. Campion, K. W. Edmonds, S. S. Dhesi, F. Maccherozzi, V. Novak, J. Wunderlich, and T. Jungwirth, Current polarity-dependent manipulation of antiferromagnetic domains, *Nature Nanotechnology* **13**, 362 (2018).
- [16] S. Y. Bodnar, L. Šmejkal, I. Turek, T. Jungwirth, O. Gomonay, J. Sinova, A. A. Sapozhnik, H. J. Elmers, M. Kläui, and M. Jourdan, Writing and reading antiferromagnetic Mn_2Au by Néel spin-orbit torques and large anisotropic magnetoresistance, *Nat. Commun.* **9**, 348 (2018).
- [17] S. Y. Bodnar, M. Filianina, S.P. Bommanaboyena, T. Forrest, F. Maccherozzi, A. Sapozhnik, Y. Skourski, M. Kläui, and M. Jourdan, Imaging of current induced néel vector switching in antiferromagnetic Mn_2Au , *Physical Review B* **99**, 140409 (2019).
- [18] M. Meinert, D. Graulich, and T. Matalla-Wagner, Electrical switching of antiferromagnetic Mn_2Au and the role of thermal activation, *Phys. Rev. Applied* **9**, 064040 (2018).
- [19] K. Olejník, T. Seifert, Z. Kašpar, V. Novák, P. Wadley, R. P. Campion, M. Baumgartner, P. Gambardella, P. Nêmec, J. Wunderlich, J. Sinova, P. Kužel, M. Müller, T. Kampfrath, and T. Jungwirth, Terahertz electrical writing speed in an antiferromagnetic memory, *Science Advances* **4**, 10.1126/sciadv.aar3566 (2018).
- [20] V. Barthem, C. Colin, H. Mayaffre, M.-H. Julien, and D. Givord, Revealing the properties of Mn_2Au for antiferromagnetic spintronics, *Nature Communications* **4**, 1 (2013).
- [21] M. Jourdan, H. Bräuning, A. Sapozhnik, H. Elmers, H. Zabel, and M. Kläui, Epitaxial Mn_2Au thin films for antiferromagnetic spintronics, *Journal of Physics D: Applied Physics* **48**, 385001 (2015).

- [22] S. Y. Bodnar, Y. Skourski, O. Gomonay, J. Sinova, M. Kläui, and M. Jourdan, Magnetoresistance effects in the metallic antiferromagnet Mn₂Au, *Phys. Rev. Applied* **14**, 014004 (2020).
- [23] P. Němec, M. Fiebig, T. Kampfrath, and A. V. Kimel, Antiferromagnetic opto-spintronics, *Nature Physics* **14**, 229 (2018).
- [24] S. A. Siddiqui, J. Sklenar, K. Kang, M. J. Gilbert, A. Schleife, N. Mason, and A. Hoffmann, Metallic antiferromagnets, *Journal of Applied Physics* **128**, 040904 (2020).
- [25] J. L. Erskine and E. A. Stern, Magneto-optic Kerr effect in Ni, Co, and Fe, *Phys. Rev. Lett.* **30**, 1329 (1973).
- [26] A. Kirilyuk, A. V. Kimel, and T. Rasing, Ultrafast optical manipulation of magnetic order, *Rev. Mod. Phys.* **82**, 2731 (2010).
- [27] T. Higo, H. Man, D. B. Gopman, L. Wu, T. Koretsune, O. M. van t Erve, Y. P. Kabanov, D. Rees, Y. Li, M.-T. Suzuki, *et al.*, Large magneto-optical Kerr effect and imaging of magnetic octupole domains in an antiferromagnetic metal, *Nature Photonics* **12**, 73 (2018).
- [28] A. S. Borovik-Romanov, A. A. Kreines, A. A. Pankov, and T. M. A, Magnetic birefringence of light in antiferromagnetic transition-metal fluorides, *Sov. Phys.-JETP* **64**, 1762 (1973).
- [29] B. B. Krichevstov and R. V. Pisarev, Anisotropy of magnetic linear dichroism in cubic magnetic substances, *Sov. Phys.-JETP* **84**, 865 (1983).
- [30] J. Ferré and G. A. Gehring, Linear optical birefringence of magnetic crystals, *Rep. Prog. Phys.* **47**, 513 (1984).
- [31] V. Saidl, P. Němec, P. Wadley, V. Hills, R. Champion, V. Novák, K. Edmonds, F. Maccherozzi, S. Dhesi, B. Gallagher, *et al.*, Optical determination of the Néel vector in a cumnans thin-film antiferromagnet, *Nature Photonics* **11**, 91 (2017).
- [32] M. Surýnek, V. Saidl, Z. Kašpar, V. Novák, R. Champion, P. Wadley, and P. Němec, Investigation of magnetic anisotropy and heat dissipation in thin films of compensated antiferromagnet CuMnAs by pump-probe experiment, *Journal of Applied Physics* **127**, 233904 (2020).
- [33] K. Yang, K. Kang, Z. Diao, A. Ramanathan, M. H. Karigerasi, D. P. Shoemaker, A. Schleife, and D. G. Cahill, Magneto-optic response of the metallic antiferromagnet Fe₂As to ultrafast temperature excursions, *Phys. Rev. Materials* **3**, 124408 (2019).
- [34] Z. Zheng, J. Y. Shi, Q. Li, T. Gu, H. Xia, L. Q. Shen, F. Jin, H. C. Yuan, Y. Z. Wu, L. Y. Chen, and H. B. Zhao, Magneto-optical probe of ultrafast spin dynamics in antiferromagnetic CoO thin films, *Phys. Rev. B* **98**, 134409 (2018).
- [35] J. Xu, C. Zhou, M. Jia, D. Shi, C. Liu, H. Chen, G. Chen, G. Zhang, Y. Liang, J. Li, W. Zhang, and Y. Wu, Imaging antiferromagnetic domains in nickel oxide thin films by optical birefringence effect, *Phys. Rev. B* **100**, 134413 (2019).
- [36] F. Schreiber, L. Baldrati, C. Schmitt, R. Ramos, E. Saitoh, R. Lebrun, and M. Kläui, Concurrent magneto-optical imaging and magneto-transport readout of electrical switching of insulating antiferromagnetic thin films, *Applied Physics Letters* **117**, 082401 (2020).
- [37] H. Meer, F. Schreiber, C. Schmitt, R. Ramos, E. Saitoh, O. Gomonay, J. Sinova, L. Baldrati, and M. Kläui, Direct imaging of current-induced antiferromagnetic switching revealing a pure thermomagnetoelastic switching mechanism in NiO, *Nano Letters* **21**, 114 (2021).
- [38] J. Xu, H. Chen, C. Zhou, D. Shi, G. Chen, and Y. Wu, Optical imaging of antiferromagnetic domains in ultrathin CoO(001) films, *New Journal of Physics* **22**, 083033 (2020).
- [39] H.-J. Elmers, S. Chernov, S. D'Souza, S. Bommanaboyena, S. Y. Bodnar, K. Medjanik, S. Babenkov, O. Fedchenko, D. Vasilyev, S. Agustsson, *et al.*, Néel vector induced manipulation of valence states in the collinear antiferromagnet Mn₂Au, *ACS nano* **14**, 17554 (2020).
- [40] S. Bommanaboyena, T. Bergfeldt, R. Heller, M. Kläui, and M. Jourdan, High quality epitaxial Mn₂Au (001) thin films grown by molecular beam epitaxy, *Journal of Applied Physics* **127**, 243901 (2020).
- [41] A. Sapozhnik, M. Filianina, S. Y. Bodnar, A. Lamirand, M.-A. Mawass, Y. Skourski, H.-J. Elmers, H. Zabel, M. Kläui, and M. Jourdan, Direct imaging of antiferromagnetic domains in Mn₂Au manipulated by high magnetic fields, *Physical Review B* **97**, 134429 (2018).
- [42] A. A. Sapozhnik, R. Abrudan, Y. Skourski, M. Jourdan, H. Zabel, M. Kläui, and H.-J. Elmers, Manipulation of antiferromagnetic domain distribution in Mn₂Au by ultrahigh magnetic fields and by strain, *physica status solidi (RRL) - Rapid Research Letters* **11**, 1600438 (2017).
- [43] S. Bommanaboyena, D. Backes, L. Veiga, S. Dhesi, Y. Niu, B. Sarpi, T. Denneulin, A. Kovacs, T. Mashoff, O. Gomonay, *et al.*, Readout of a antiferromagnetic spintronics systems by strong exchange coupling of Mn₂Au and permalloy, *arXiv preprint arXiv:2106.02333* (2021).
- [44] L. Nadvorník, M. Borchert, L. Brandt, R. Schlitz, K. A. de Mare, K. Výborný, I. Mertig, G. Jakob, M. Kläui, S. T. Goennenwein, *et al.*, Broadband terahertz probes of anisotropic magnetoresistance disentangle extrinsic and intrinsic contributions, *Phys. Rev. X* **11**, 021030 (2021).
- [45] H. S. Carslaw and J. C. Jaeger, *Conduction of heat in solids* (Clarendon press, 1992).
- [46] D. Mihailovic and J. Demsar, Time-resolved optical studies of quasiparticle dynamics in high-temperature superconductors: Experiments and theory, in *Spectroscopy of Superconducting Materials* (American Chemical Society, 1999) Chap. 16, pp. 230–244.
- [47] S. Burghartz and B. Schulz, Thermophysical properties of sapphire, AlN and MgAl₂O₄ down to 70 K, *Journal of nuclear materials* **212**, 1065 (1994).
- [48] S. Bodnar, *Manipulation of Néel Vector in Antiferromagnetic Mn₂Au by Electric Current and Magnetic Field Pulses*, Ph.D. thesis, Johannes Gutenberg-Universität Mainz (2020).
- [49] W. M. Yim and R. J. Paff, Thermal expansion of AlN, sapphire, and silicon, *Journal of Applied Physics* **45**, 1456 (1974).
- [50] C. Roder, S. Einfeldt, S. Figge, T. Paskova, D. Hommel, P. P. Paskov, B. Monemar, U. Behn, B. A. Haskell, P. T. Fini, and S. Nakamura, Stress and wafer bending of a-plane GaN layers on r-plane sapphire substrates, *Journal of Applied Physics* **100**, 103511 (2006).